Chemical Science

Accepted Manuscript

This article can be cited before page numbers have been issued, to do this please use: L. K/Bidi, T. Rocca, L. Chen, A. Gutierrez Schindler, B. Limoges and V. Balland, *Chem. Sci.*, 2026, DOI: 10.1039/D6SC00393A.

ROYAL SOCIETY OF CHEMISTRY

rsc.li/chemical-science

View Article Online
DOI: 10.1039/D6SC00393A

ARTICLE

How Solvent Activity and Solute Solvation Control Electrode Potentials: Quantitative Insights from Li^+ Insertion into TiO_2

Received 00th January 20xx,
Accepted 00th January 20xx

DOI: 10.1039/x0xx00000x

Ludivine K/Bidi, Tom Rocca, Lucie Chen, Andrea Gutierrez Schindler, Benoît Limoges,* Véronique Balland*

Tuning electrolyte salt concentration has emerged as a powerful strategy to enhance the performance of rechargeable batteries by mitigating parasitic side reactions. Here, we introduce a unified and quantitative validation of an electrolyte thermodynamic framework incoporated into a modified Nernst equation that explicitly includes electrolyte-specific parameters—namely, salt and solvent activities, as well as the salt hydration number—to rationalize and predict how electrode potentials vary with electrolyte concentration in reversible ion-insertion systems. We demonstrate this generic methodology for reversible Li^+ insertion into anatase TiO_2 using aqueous LiCl electrolytes. By combining tabulated water and LiCl activities with concentration-dependent hydration numbers derived from both experimental and theoretical approaches, we achieve quantitative agreement between predicted and measured potential shifts. This work establishes a reliable and broadly applicable framework for deciphering and controlling electrolyte-concentration effects in batteries and, more generally, in electrochemical systems involving concentrated electrolytes.

Introduction

Electrolyte composition is a key determinant of both the performance and lifetime of rechargeable batteries.[1] Not only does it govern ion transport, conductivity, but it also fundamentally controls the thermodynamics and kinetics of interfacial electrochemical processes. These interfacial processes include reversible ion insertion into host materials and controlled electrodeposition of metals at current collectors. Electrolyte formulation is also essential for establishing a stable solid-electrolyte interphase (SEI) and suppressing undesirable side reactions such as degradation, dissolution, and corrosion of active materials. Furthermore, appropriate electrolyte selection mitigates dendrite growth during metal electrodeposition and reduces parasitic hydrogen or oxygen evolution reactions in aqueous systems.

Traditionally, electrolyte design has relied on molar salt concentration to balance ionic conductivity and viscosity. However, recent advances have shown that increasing salt concentrations can profoundly alter ion solvation structures and interfacial reactivities,[2-4] especially for aqueous electrolytes spanning dilute to "water-in-salt" (WiS) regimes. WiS electrolyte (WiSE) formulations, characterized by a low water-to-cation ratio and an anion-rich environment, have been particularly effective for expanding the electrochemical stability window (up to ~3 V) by reducing water activity[5, 6] and thereby suppressing both water reduction and oxidation.[7] This enables the reversible cycling of low-potential anodes such as Mo_6S_8, TiO_2 or $Li_6Ti_5O_{12}$ (LTO),[7-9] thereby opening pathways to high-energy-density aqueous batteries. Concentrated electrolytes also significantly impact the thermodynamics of ion insertion and metal electrodeposition. For instance, high lithium-ion concentrations in non-aqueous systems enable highly reversible lithium plating/stripping[10] and graphite intercalation.[11-16] This behaviour is attributed to an unusual upshift in the equilibrium potential of metal electrodeposition or ion-insertion, which reduces the driving force for side reactions (such as dendrite formation or graphite exfoliation), and thereby enhances reversibility. Comparable potential shifts have been observed for many insertion compounds (*e.g.*, $LiFePO_4$, $LiCoO_2$, LTO) in both non-aqueous[17] and aqueous electrolytes,[18-20] as well as for various metal ions insertion[21] or deposition processes.[22-26] These findings suggest a generic phenomenon fundamentally rooted in the physicochemical properties of the electrolyte, with applications extending well beyond the field of rechargeable batteries, as recently illustrated by electrochemical Li-mediated nitrogen reduction for sustainable ammonia synthesis,[27] lithium-ion battery recycling,[28] and facilitated electrocatalytic reduction of CO into C_2H_4.[29] All these underscore the need to quantitatively understand how electrolyte nature, composition, and concentration govern the electrode potential.

To address this, Yamada and co-workers proposed a computational framework to determine the total free energy of solvated Li^+ ions across concentrations.[17, 21] This method, based on molecular dynamics simulations that sum short-range Coulombic interactions within the Li^+ solvation shell, allows to reproduce experimental potential shifts (>0.3 V) for Li^+ insertion and Li metal electrodeposition. However, this computational approach is demanding and less intuitive regarding the underlying physicochemical factors driving the potential shifts. A classical physicochemical model that captures electrolyte thermodynamics and links directly to the Nernst equation offers assuredly a more accessible alternative. However, for that purpose, it is necessary to formulate a relevant Nernst expression for the electrochemical process under consideration.

If we consider the case of reversible insertion of Li^+ into an active material, the latter can be described by the following cation-insertion coupled electron-transfer reaction at the electrode/electrolyte interface (assuming an ideal host lattice with equivalent, non-interacting insertion sites):

[a] *Université Paris Cité, CNRS, ITODYS, F-75013 Paris, France*
† Footnotes relating to the title and/or authors should appear here.

$$\theta + e^- + Li(S)_n^+ \rightleftharpoons \theta_{Li} + n\,S \quad (1)$$

where θ is the fraction of unoccupied insertion sites (oxidized states) converted to θ_{Li} (reduced states) through the coupled insertion of desolvated Li^+ from solvated $Li(S)_n^+$, with n solvating solvent molecules being released during reduction and re-associated upon oxidation. The Nernst potential E (in V) is then given by:

$$E = E^0_{\theta,Li(S)_n^+/\theta_{Li}} + \frac{RT}{F}\ln\frac{\theta}{\theta_{Li}} + \frac{RT}{F}\ln\frac{a_{Li(S)_n^+}}{a_s^n} \quad (2)$$

where $E^0_{\theta,Li(S)_n^+/\theta_{Li}}$ is the standard potential of the insertion material (in V *vs*. a given reference electrode, with the standard state defined for a material at half state of charge and a solute at a 1 mol·kg^{-1} or 1 M under putative infinite dilution conditions), $a_{Li(S)_n^+}$ the activity of solvated Li^+, and a_s the activity of solvent. This expression explicitly accounts for the n solvent molecules acting as co-reactants, a contribution that is often neglected.[20, 30, 31] Omitting this term is equivalent to incorrectly assume that, regardless of concentration, $a_s = 1$, thereby leading to misinterpretations of potential shifts.

For $\theta_{Li} = 0.5$ and using the convention that $a_{Li(S)_n^+} = a_{LiX} = \gamma_{LiX} C_{LiX}$ (with γ_{LiX} and C_{LiX}, the mean ionic activity coefficient and concentration of the LiX salt),[32] eq. 2 then leads to the following half equilibrium potential:

$$E_{1/2} = E^0_{\theta,Li(S)_n^+/\theta_{Li}} + \frac{RT}{F}\ln(\gamma_{LiX} C_{LiX}) - n\frac{RT}{F}\ln(a_s) \quad (3)$$

Applying these Nernst equations (*i.e.*, eqs. 2 or 3) correctly poses several significant challenges. The first concerns the accurate estimation of salt and solvent activities. It is worth noting that similar Nernst-type expressions have been employed to interpret the potential shifts of Li^+ intercalation into graphite from molten glymes-Li salt mixtures[16, 33] and during Li plating as a function of LiTFSI or LiFSA concentration in non-aqueous solvents.[33-35] However, in all these studies, the activities of Li^+ and of the free solvent were approximated by their concentrations—a simplification that becomes invalid in concentrated electrolytes. Another difficulty lies in assigning an appropriate value to n, which is expected to vary with the nature of salt and solvent, and with the electrolyte concentration. A further complication arises from the potential shift due to the liquid junction potential ($\Delta\phi_j$) generated across the salt bridge of the reference electrode. Although numerous theoretical approaches exist to estimate this potential, none are fully satisfactory.[32] Nevertheless, given that many studies report maximal $\Delta\phi_j$ values on the order of a few tens of mV,[20, 32, 36-38] this contribution can be regarded as negligible in the context of the present work.

To demonstrate the applicability of Nernst eq. 3 to a well-defined illustrative system, we considered here the reversible insertion of Li^+ into TiO_2 (anatase) from dilute to saturated aqueous LiCl electrolytes. An advantage of using aqueous LiCl electrolytes is their well-established thermodynamic properties and the very high solubility of LiCl in water, allowing to easily access WiS regimes. To experimentally determine how the solvation number n (or hydration number h in water) evolves with the electrolyte concentration, we employed a ratiometric Raman analysis of the hydration shell.[39] Moreover, to support the validity of our experimental analysis, the thermodynamic properties of LiCl solutions were modeled on the basis of a recently developed speciation-based solution model[40-42] capable of relating the solution vapor pressure (solvent activity) to the modeled solute and solvent speciated concentrations. This approach enables accurate prediction of the water activity (a_w), solute activity (a_{LiCl}), and hydration number (h) up to saturation.

Results and discussion

Reversible Li^+ insertion equilibrium potentials into anatase were obtained from cyclic voltammograms (CVs, Figure 1a-c) recorded in aqueous LiCl electrolytes (0.5 to 18 mol·kg^{-1}) at various anatase-based electrodes, *i.e.* (*i*) composite electrodes made of 80 wt% anatase nanoparticles (5 or 25 nm), 10 wt% carbon, and 10 wt% Nafion binder on titanium current collectors, and (*ii*) 3D nanostructured pure anatase films (1 µm-thick) on Ti-coated glass.[43, 44] The three-electrode cell included a Ag/AgCl (saturated KCl) reference and a Pt counter electrode. A slow scan rate of 1 mV·s^{-1} was used to ensure near-thermodynamic control. As shown in Figure 1d, the extracted half-wave potentials, $E_{1/2}$ (average anodic/cathodic peaks,

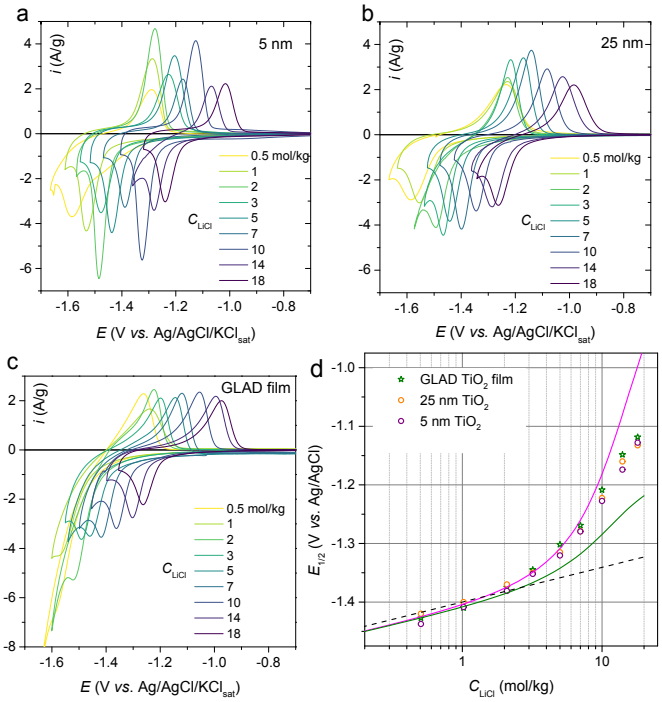

Fig. 1 Potential shifts in CV as a function of LiCl concentration. (a-c) CVs of anatase electrodes recorded at 1 mV·s^{-1} in aqueous LiCl electrolytes with molalities ranging from 0.5 to 18 mol·kg^{-1} (see legends on graphs). The anatase electrodes were (a, b) porous composite electrodes containing 80 wt% of (a) 5 nm or (b) 25 nm anatase nanoparticles, and (c) nanostructured anatase films (1-µm-thick) deposited on Ti-coated glass. (d) Semilogarithmic plots of $E_{1/2}$ as a function of LiCl concentration. Open dot and star symbols: $E_{1/2}$ values extracted from the CVs in panels a-c. The dashed and solid curves correspond to plots of Nernst eq. 3 (using $E^0_{\theta,LiH_2O^+/\theta}$ = -1.4 V) under different conditions: dashed black line, ideal case with $\gamma_{LiCl} = 1$ and $a_w = 1$; solid green curve, γ_{LiCl} values taken from literature (also reported in Figure 2) and $a_w = 1$; magenta solid curve, full dependence of γ_{LiCl} and a_w on LiCl concentration (see Figure 2), including the solvation number n (or h) adjusted to 4.5.

which is assumed to be close to the half equilibrium potential governed by eq. 3), evolved identically with LiCl concentration across all electrodes, regardless of their morphology, reflecting complete dependence on the electrolyte's thermodynamic properties. As a result, one can anticipate that the $E_{1/2}$ evolution as a function of LiCl concentration can be quantitatively reproduced from Nernst eq. 3 and from the knowledge of γ_{LiCl} (an thereby a_{LiCl}), a_w, and hydration number h.

Experimental values of a_w and γ_{LiCl} at 25°C for LiCl molalities ranging from 0.1 mol·kg^{-1} to saturation are available from compiled literature data (plots shown in Figure 2).[45] Using these data, the $E_{1/2}$ evolution was calculated with eq. 3. By adjusting the hydration number h (where $n = h$) to a constant value of 4.5 and using $E^0_{\theta,Li(H_2O)^+_h/\theta_{Li}}$ = -1.4 V, the resulting curve (magenta) in Figure 1d closely matches the experimental $E_{1/2}$ at low LiCl concentrations (below 7 mol·kg^{-1}). This h = 4.5 value aligns with literature reports for dilute lithium salt solutions, where various experimental and theoretical approaches consistently estimate an average of 4–6 water molecules per lithium ion.‡, [46-49]

It is worth noting that if only the activity of LiCl is considered in the Nernst equation (setting the solvent activity to 1, *i.e.* a_w = 1), it leads to the green curve in Figure 1d which fails to reproduce the experimental data, except at the lowest concentrations. This result indirectly underscores the importance of accounting for the contribution of water activity raised to the power h in Nernst eq. 3 (with $n = h$). Finally, the black dashed line in Figure 1d corresponds to the case where a_w = 1 and γ_{LiCl} = 1, representing ideal dilute conditions in which only the LiCl concentration contributes.

From the theoretical magenta plot in Figure 1d, it is evident that at the highest concentrations, the curve diverges from the experimental trend, increasing more rapidly. This behavior is consistent with the progressive depletion of free water molecules available to fully hydrate the solute, specifically Li^+ ions.‡, [50] Indeed, at high salt concentrations, the number of water molecules becomes insufficient to maintain a constant hydration number of 4.5. A simple calculation shows that at approximately 12 mol·kg^{-1} LiCl, the 55 mol of water present are not enough to ensure fully hydrated ions. This thus highlights the need to determine how the hydration number h evolves with the electrolyte concentration, which we investigated using both experimental and theoretical approaches.

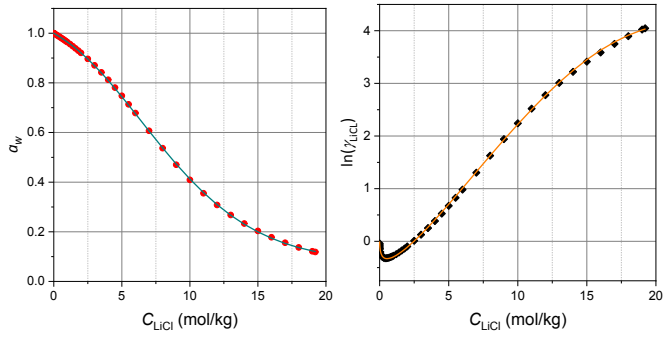

Fig. 2 Water activity and mean ionic activity coefficient of LiCl solutions. Solid dots: experimental (left) water activity and (right) mean ionic activity coefficient of LiCl as a function of concentration (from ref. 45). Solid curves: best fits of the thermodynamic speciation-based solution model to the experimental data using K_h = 5.46, m = 2.21, K_{id} = 0.45, and r_i = 0.53 nm, see text.

Given the complexity of solvation phenomena in concentrated electrolytes, it is useful to clarify the physical meaning of the hydration number h employed in this work before discussing its evolution with electrolyte concentration. The hydration number h is here defined as an average effective solvation number, representing the mean number of water molecules interacting with the solute species through sufficiently strong ion–dipole or hydrogen-bond interactions to be distinguished from bulk (free) water. This definition therefore extends beyond the strict first coordination shell and accounts for the dynamic exchange between tightly and loosely bound water molecules. The quantity h thus corresponds to an averaged value encompassing all solute-related species present in solution, including free ions and ion pairs, which naturally integrates the effects of ion pairing and aggregation without the need to assign separate hydration parameters to each species. Within this formulation, the decrease of h with increasing electrolyte concentration reflects both the consumption of solvent molecules for solvation and the progressive formation of contact and solvent-shared ion pairs in concentrated and water-in-salt regimes.

Hydration numbers of ions in aqueous media can be evaluated using various spectroscopic methods[46, 51] such as neutron or X-ray diffraction, Raman spectroscopy, NMR, as well as by measurements of solution compressibility[52] or theoretical chemistry computations.[53] However, many of these methods have primarily determined hydration numbers under so-called infinite dilute conditions and have rarely assessed the evolution of h with solute concentration.[52, 54] Among these techniques, solution Raman spectroscopy is particularly attractive due to its accessibility. Therefore, we have used it to experimentally determine h over a range of LiCl electrolyte concentrations, taking advantage of the OH stretching band change at 2 800 – 3 700 cm^{-1} and using the ratiometric methodology proposed by Wang *et al.*[39] to extract hydration-shell Raman spectra, which reflects the structural features of the hydration shell.

Briefly, given that the LiCl salt makes no direct contribution to the O-H streching band, the Raman spectra, in the 2800-3700 cm^{-1} region (Figure 3a), only relies on a linear combination of the spectra corresponding to bulk (or free) water molecules (*i.e.* $I_{bulk}(\nu)$, equivalent to the spectra of pure water) and water molecules in the solute hydration shell (*i.e.* $I_{hydration}(\nu)$):

$$I_{solution}(\nu) = I_{bulk}(\nu) + I_{hydration}(\nu) \quad (4)$$

Upon increasing the salt concentration, the intensity below 3200 cm^{-1} progressively decreases (Figure 3a). This trend reflects a diminution of the number of water molecules involved in double donor-double acceptor hydrogen bonding, which constitute one of the dominant hydrogen-bond motifs in pure water, and is associated to large water clusters.[55] It clearly reflects the consumption of solvent molecules by solvation as the salt concentration increases. This spectroscopic evolution provides direct experimental support for the thermodynamic framework developed in the following section, which quantitatively relates the variation of solvent activity and the effective solvation number to the concentration-dependent behaviour of the electrolyte.

Raman ratio spectra calculated for each salt concentration were used to extract the proportionality coefficient linking $I_{bulk}(\nu)$ to the spectra of pure water (see SI for details and Figure S1).

Next, the Raman spectra of both bulk and hydration-shell water molecules can be determined, as shown in Figure 3b for the

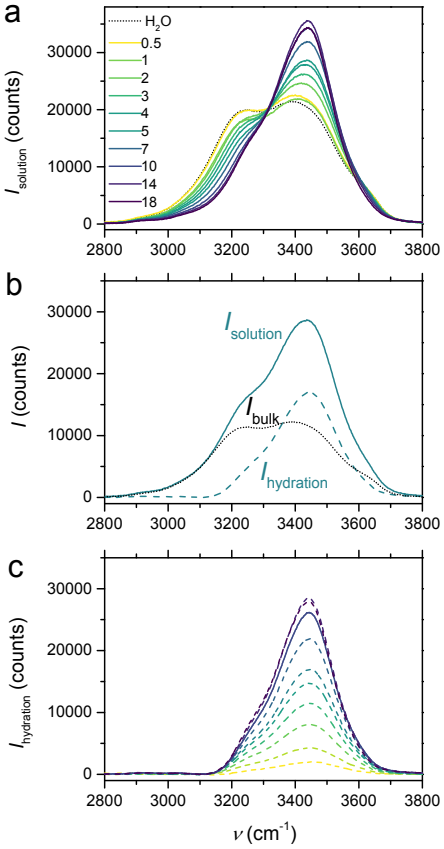

Fig. 3 Raman spectra analysis of the aqueous LiCl electrolytes in the 2800–3100 cm^{-1} region: (a) solution spectra of pure water (dotted gray line) and LiCl electrolytes with concentrations ranging from 0.5 to 18 $mol \cdot kg^{-1}$ (solid yellow to dark lines); (b) deconvolution of the solution spectra (solid lines) into bulk-like (dotted lines) and hydration-shell (dashed lines) components (at 5 $mol \cdot kg^{-1}$); (c) hydration-shell spectra for all electrolyte concentrations (same code color as in a).

5 $mol \cdot kg^{-1}$ LiCl electrolyte, and Figure 3c for the hydration-shell spectra determined at all salt concentrations. These spectra account for any solvent molecules whose vibrational spectra are significantly perturbed by the solute. From their integration, the number of water molecules in the hydration shell (*i.e.*, $n_{hydration}$) can be estimated, allowing in turn to access the hydration number h, being defined as $h = n_{hydration} / n_{solute}$.

The hydration number h is finally given by the following expression:

$$h = \frac{\int I_{hydration}(\nu)\,d\nu}{\int I_{hydration}(\nu)\,d\nu + \frac{\sigma_{hydration}}{\sigma_{pure}} \int I_{bulk}(\nu)\,d\nu} \Bigg/ \frac{n_{LiCl}}{n_{water}} \qquad (5)$$

where $\sigma_{hydration}$ and σ_{pure} are the Raman scattering cross section corresponding to hydration shell and pure water molecules, determined as described in the SI.

The h values thus extracted (red diamonds in Figure 4a) show a continuous decline with increasing LiCl molality, starting from an initial value of ~4.5 at low concentrations to a minimum of about 1.7 near saturation (18 $mol \cdot kg^{-1}$). Injecting these h values along with the corresponding a_w and γ_{LiCl} values (inferred from

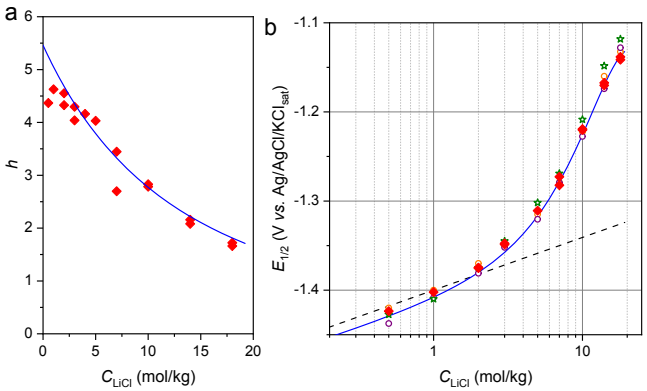

Fig. 4 Estimation of the hydration number h and its impact on $E_{1/2}$. (a) Average hydration number as a function of LiCl molality. Solid red diamonds: data from solution Raman spectroscopy (see SI for details). Solid blue line: theoretical curve obtained from the speciation-based solution model. (b) Semilogarithmic plots of $E_{1/2}$ as a function of LiCl concentration. Open dot and star symbols: same experimental data as in Figure 1d. Dashed black line: theoretical Nernst eq. 3 under ideal conditions (*i.e.*, $a_w = 1$ and $\gamma_{LiCl} = 1$). Solid red diamonds: Nernst eq. 3 using dependences of a_w and γ_{LiCl} on LiCl concentration (Figure 2), plus hydration number h from Raman spectroscopy (panel a). Solid blue line: Nernst eq. 3 plotted using the values of a_w, γ_{LiCl}, and h modeled from the speciation-based solution model (using K_h = 5.46, m = 2.21, K_{id} = 0.45, and r_i = 0.53 nm, see text).

Figure 2) into eq. 3 yields, for each tested LiCl concentration, the red diamonds in Figure 4b. The excellent overlap of the calculated and experimental $E_{1/2}$ potentials clearly validates our approach.

To advance further, we employed the speciation-based solution model recently proposed by Wilson and coworkers[40-42] in order to reproduce the non-ideal variations of water and solute activities as a function of LiCl concentration, and also to provide the associated concentration-dependent hydration number. Moreover, to account not only for short-range ion-solvent interactions (*via* stepwise hydration equilibria under the law of mass action) and ion pairing, as proposed by Wilson and coworkers,[40, 42] the model was extended to include long-range electrostatic contributions through Debye-Hückel theory.

Grounded in mechanistic principles, this model requires only a minimal set of 4 adjustable parameters: a composite hydration equilibrium constant K_h, a hydration modifier m, an ion-pair dissociation constant K_{id}, and the mean ionic radius r_i of the solute.

A primary key assumption of the model is that the experimental activity of water a_w defined by the solution vapour pressure, p, relative to the pure water at the same temperature, p^0, directly correspond to the mole fraction of free-water, x_w^{free}:[40]

$$a_w = \frac{p}{p^0} = x_w^{free} \qquad (6)$$

Based on this assumption, the mole fraction of a 1:1 MX speciated solute i, *i.e.* x_i^{spe}, can be found through the water activity residual:

$$1 - a_w = x_i^{spe} \qquad (7)$$

The secondary key assumption of the model is that ion hydration proceeds *via* step-wise hydration equilibria that can be aggregated, simplified, and expressed as the following relationship for the speciated (hydrated) solute concentration, x_i^h (in mole fraction):[42]

$$x_i^h = \frac{x_i}{x_w - hx_i + x_i} = \frac{x_i}{1 - hx_i} \quad (8)$$

where x_i and x_w are the absolute mole fractions of solute *i* and water *w*, respectively, the latter being given for a fully dissociated 1:1 MX salt in water by:

$$x_i = \frac{2C_i}{55.509 + 2C_i} \quad (9)$$

$$x_w = 1 - x_i = \frac{55.509}{55.509 + 2C_i} \quad (10)$$

with C_i the molality of the salt in solution, and 55.509 the number of moles of water contained in 1 kg.

In eq. 8, the hydration number *h* is a function of the water mole fraction, as follows:[42]

$$h = K_h x_w{}^m \quad (11)$$

with K_h the composite hydration association constant and *m* the hydration modifier. This expression defines hydration as being exponentially proportional to the mole fraction of water through the parameter *m*. A second-order hydration term, *i.e.* *m* = 2, is generally sufficient to accurately model the electrolyte behavior from dilute conditions up to saturation.[42]

To account for the fact that certain salts exhibit a degree of ion pairing, the following hydrated solute equilibrium has to be considered:

$$M^+_{hyd} + X^-_{hyd} \rightleftarrows MX_{hyd}$$

This equilibrium is governed by the following dissociation equilibrium constant, K_{id} (expressed here in terms of activities in the mole fraction scale):

$$K_{id} = \frac{a_M a_X}{a_{MX}} \quad (12)$$

where a_M , a_X , a_{MX} are the activities of the speciated cation M^+, anion X^-, and ion-pair MX.

In this context, the mole fractions of the partially dissociated and hydrated species (*i.e.*, cation M^+, anion X^-, and ion-pair MX species) must be expressed as follows: [¥]

$$x_M^{h,K} = \frac{\alpha C_i}{55.509 - h(1+\alpha)C_i + (1+\alpha)C_i} \quad (13)$$

$$x_X^{h,K} = \frac{\alpha C_i}{55.509 - h(1+\alpha)C_i + (1+\alpha)C_i} \quad (14)$$

$$x_{MX}^{h,K} = \frac{(1-\alpha)C_i}{55.509 - h(1+\alpha)C_i + (1+\alpha)C_i} \quad (15)$$

where α is the degree of dissociation of the salt.

Assuming in eq 12 that each activity *a* is equal to the "true" mole fractions $x^{h,K}$ of the partially dissociated and hydrated species, then the equilibrium constant can be written:

$$K_{id} = \frac{x_M^{h,K} x_X^{h,K}}{x_{MX}^{h,K}} = \frac{\alpha^2}{(1-\alpha)} \frac{C_i}{55.509 - h(1+\alpha)C_i + (1+\alpha)C_i} \quad (16)$$

with α determined by:

$$\alpha = \frac{55.509K_{id} - \sqrt{\Delta}}{2C_i(K_{id}h - K_{id} - 1)} \quad (17)$$

and $\Delta = (55.509K_{id})^2 - 4K_{id}C_i(K_{id}h - K_{id} - 1)(55.509 - hC_i + C_i)$.

From the determination of α, it becomes thus possible to calculate the mole fractions $x_M^{h,K}$, $x_X^{h,K}$, and $x_{MX}^{h,K}$, as well as $x_i^{h,K}$ from:

$$x_i^{h,K} = x_M^{h,K} + x_X^{h,K} + x_{MX}^{h,K} \quad (18)$$

Using eq. 18, one can thus obtain the mole fraction of free solvent: $x_w^{h,K} = 1 - x_i^{h,K}$.

At this stage, the long-range electrostatic contribution on the hydrated and partially dissociated solute can be introduced into the model through the following modification of water activity by the Debye-Hückel term, K_w^{DH}:[41]

$$x_w^{h,K,DH} = 1 - x_i^{h,K,DH} = \frac{x_w^{h,K}}{K_w^{DH}} = \frac{1 - x_i^{h,K}}{K_w^{DH}} \quad (19)$$

with $K_w^{DH} = \exp\left(-\frac{2A_x I^{3/2}}{1 + r_i B_x I^{1/2}}\right)$.

Here, $A_x = 2.917$ and $B_x = 24.4$ are the Debye-Hückel constants (at 298 K) in the mole fraction scale, r_i is a parameter related to the average ionic size of the solute, and *I* is the ionic strength of the electrolyte calculated from the mole fraction of hydrated and partially dissociated solute (wherein MX contribution is null because $z_{MX} = 0$):

$$I = \frac{1}{2}\sum\left(x_M^{h,K} z_M{}^2 + x_X^{h,K} z_X{}^2 + x_{MX}^{h,K} z_{MX}{}^2\right) \quad (20)$$

The resulting modeled free water activity, *i.e.* $x_w^{h,K,DH}$ (thus equivalent to x_w^{free} in eq. 6), can then be used to fit either the experimental data of a_w or the mean solute activity coefficient γ_i (by using first eq. 21 for calculating the osmotic coefficient ϕ in the absolute molal scale of C_i and then using eq. 22 to calculate γ_i knowing ϕ) through iterative adjustments of K_h, *m*, K_{id}, and r_i.

$$\phi = -55.509\frac{\ln\left(x_w^{h,K,DH}\right)}{2C_i} \quad (21)$$

$$-\ln\gamma_i = (1-\phi) + \int_0^{C_i}\frac{(1-\phi)}{C_i}dC_i \quad (22)$$

From the best fits (see Figure 2), the following values were obtained: K_h = 5.46, *m* = 2.21, K_{id} = 0.45, and r_i = 0.53 nm.

The K_{id} value is in the order of magnitude of that determined experimentally,[56] while the values of K_h and *m* are close to those previously reported by Wilson and coworkers.[42] Regarding the value of r_i, it aligns with expectations for the average ionic radius of hydrated ions, noting that within Debye-Hückel theory, this parameter is generally treated as flexible and non-physical. Knowing K_h and *m*, the evolution of *h* as a function of C_{LiCl} can be plotted from eq. 11 (blue plot in Figure 4a). The calculated trend almost perfectly matches the experimental Raman data. This remarkable agreement between two independent approaches—solution Raman spectroscopy and water activity modeling—strongly supports our quantitative determination of *h* evolution with C_{LiCl}. On this basis, the variation of $E_{1/2}$ was subsequently determined from eq. 3 using

the values of a_w, γ_i, and h, directly obtained from the model. This yields the blue curve in Figure 4b, which nearly overlaps the experimental data. This strong agreement unambiguously validates our approach and, in particular, the proposed Nernst-type equation, which—when combined with an appropriate thermodynamic model—provides a consistent, quantitative prediction of how the insertion potential of a cation evolves with electrolyte concentration. The good overlap of both the Raman-based and model-based plots with the experimental data in Figure 4b also indirectly confirms that the potential junction contribution to the potential shift can be considered as negligible.

With this improved understanding of the key electrolyte parameters governing the electrode potential associated with ion insertion into a material, we can better rationalize how to mitigate undesirable competing side reactions. This is clearly illustrated by the CVs in Figure 1c. As the LiCl concentration increases, the reversible Li^+ insertion wave into TiO_2 progressively shifts toward more positive potentials, whereas the irreversible and undesirable hydrogen evolution reaction remains nearly unaffected, as its reduction potential changes only slightly (thermodynamically) with LiCl concentration (as attested by the electrolyte pH which remains almost constant—see Table S1 in SI). This insight largely explains the superior Coulombic efficiencies reported for numerous materials in WiSEs.[2, 7, 8, 9, 57, 58]

Conclusion

In this work, we present a rigorous unification and quantitative validation of electrolyte thermodynamics in insertion systems to rationalize the anomalous evolution of the potential of an insertion material as a function of electrolyte concentration, spanning dilute regimes up to water-in-salt conditions. We demonstrate that the Nernst equation can quantitatively describe the variation of electrode potential, provided that both the salt mean activity and the solvent activity, raised to a power corresponding to the electrolyte hydration number, are properly considered. We further show how a decrease in the hydration number influences the electrode potential in the WiS regime, and how this quantity can be accessed experimentally, through Raman spectroscopy, or theoretically, via electrolyte modelling approaches.

By focusing on a 1:1 electrolyte, this study lays the groundwork for the subsequent interpretation of potential shifts observed in more complex electrolyte systems, including those exhibiting richer solution speciation, bi-salt formulations, or the presence of co-solvents. Developing a comprehensive understanding of how electrolyte composition and concentration govern electrode potential remains a key contemporary challenge, central to the rational design of advanced electrochemical devices for energy storage and beyond.

Experimental Section

Chemicals. Anhydrous lithium chloride (free-flowing, Redi Dri™, ACS reagent, ≥ 99%) was purchased from Sigma-Aldrich/Merck. Nafion D-520 (5 wt. % in a mixture of lower aliphatic alcohols and water) was obtained from Sigma-Aldrich/Merck. Ketjenblack EC-600JD was supplied by Nanografi Nano Technology. TiO_2 anatase nanopowder (< 25 nm diameter) were purchased from Sigma-Aldrich, and TiO_2 pure anatase nanoparticles (5 nm diameter) were obtained from NanoAmor (USA). All aqueous solutions were prepared with Milli-Q water (18.2 MΩ·cm).

Electrodes. Anatase GLAD-TiO_2 electrodes were prepared as previously described.[43] Composite electrodes were fabricated from a slurry consisting of 80 wt% active material, 10 wt% Ketjenblack EC-600JD, and 10 wt% Nafion. The active material and carbon were first dispersed in the Nafion suspension. Approximately 100 µL of Milli-Q water was then added to obtain a homogeneous ink. The suspension was stirred for 2 h and cast onto titanium sheets (0.127 nm thickness) using a manual Elcometer 3520 Baker film applicator adjusted to a 200 µm height. The electrodes were dried at ambient temperature and pressure. The mass loading of active material was 1.7 to 2 $mg \cdot cm^{-2}$.

Electrochemical measurements. Cyclic voltammetry was performed in a standard three-electrode cell using a BioLogic VSP potentiostat controlled by EC-Lab software. A platinum wire served as the counter electrode, and an Ag/AgCl (saturated KCl) electrode was used as the reference. Prior to measurements, the electrolyte was degassed for 20 min, and a constant argon flow was maintained above the solution throughout the experiments. Current densities were calculated by normalizing the measured current to the mass of active material in the electrode. All potentials are reported *vs.* Ag/AgCl (saturated KCl).

Electrolyte characterization. All measurements were performed at 22°C. Conductivity and pH measurements were measured with an Accumet XL200 benchtop meter (Fisher Scientific) calibrated using standard buffer and KCl solutions before each use. Water activity was determined using an AQUALAB 4TE chilled-mirror dew-point hygrometer (precision ±0.003). Solution densities were estimated using a 5 mL volumetric flask. All data are reported in Table S1.

Raman spectroscopy was carried out using a LabRAM HR 800 high-resolution Raman microspectrometer operating over 2500-4180 cm^{-1} spectral range. A He–Ne laser (λ = 633 nm) delivering 8 mW at the sample was used as the excitation source. The spectrometer was coupled to an optical microscope equipped with a 10× objective (N.A. = 0.25) focused on a horizontal optical cuvette with a 2 mm optical path. Measurements were performed under air at 25°C. Two sets of electrolytes were analyzed, with each spectrum acquired with an integration time of 15 s or 20 s and 20 accumulations to improve the signal-to-noise ratio. Baseline correction of the Raman spectra was performed using Labspec 6 software. Typically, a fourth-order polynomial was fitted to subtract the background. When the automatic baseline algorithm did not provide a satisfactory fit, additional baseline points were manually selected.

Conflicts of interest

There are no conflicts to declare.

Data availability

View Article Online
DOI: 10.1039/D5SC00393A

The data supporting this article have been included as part of the Supplementary Information. Supplementary information (SI): Raman analysis, Tables S1 and S2, Figures S1 and S2. The data and calculations that support the findings of this study are available from the corresponding author upon request.

Acknowledgements

This work was partially supported by the Paris Ile-de-France Region in the framework of DIM MaTerReE. The authors thank Stéphanie Lau-Truong and Kenneth Harris for assistance in Raman spectra acquisitions and the preparation of GLAD electrodes, respectively. The authors thank the Agence Nationale pour la Recherche (ANR) for its financial support (RePIB project - ANR-25-CE50-2673-01).

Notes and references

‡ According to experimental evidence, in many aqueous electrolytes cations are considered more extensively hydrated (or solvated) than anions.

¥ Compared to Wilson's model,[40-42] the ion-pairing equilibrium was treated differently by expressing solute hydration in terms of partially dissociated species (*i.e.*, $(1+\alpha)C_i$) rather than fully dissociated ones (*i.e.*, $2C_i$), which avoids approximation and ensures that the dissociation constant K_{id} remains strictly constant regardless of solute concentration, thus preserving compliance with the law of mass action.

1 K. Xu, Electrolytes and Interphases in Li-Ion Batteries and Beyond. *Chem. Rev.,* 2014, **114**, 11503–11618. (DOI: 10.1021/cr500003w).

2 O. Borodin, J. Self, K. A. Persson, C. Wang and K. Xu, Uncharted Waters: Super-Concentrated Electrolytes. *Joule,* 2020, **4**, 69–100. (DOI: 10.1016/j.joule.2019.12.007).

3 H. Cheng, Q. Sun, L. Li, Y. Zou, Y. Wang, T. Cai, F. Zhao, Liu G., Z. Ma, W. Wahyudi, Q. Li and J. Ming, Emerging Era of Electrolyte Solvation Structure and Interfacial Model in Batteries. *ACS Energy Lett.,* 2022, **7**, 490–513. (DOI: 10.1021/acsenergylett.1c02425).

4 Y. Ugata, K. Shigenobu, R. Tatara, M. Watanabe and K. Dokko, Solvate electrolytes for Li and Na batteries: structures, transport properties, and electrochemistry. *Phys. Chem. Chem. Phys.,* 2021, **23**, 21419–21436. (DOI: 10.1039/D1CP02946K).

5 Y. Zhigalenok, S. Abdimomyn, M. Levi, N. Shpigel, M. Ryabicheva, M. Lepikhin, A. Galeyeva and F. Malchik, Water activity: the key to unlocking high-voltage aqueous electrolytes? *J. Mater. Chem. A,* 2024, **12**, 33855. (DOI: 10.1039/D4TA06655C).

6 D. G. Vazquez, J. Ingenmey, K.A. Trapp, D. Ciliak, M. Salanne and M.R. Lukatskaya, Extended Stability Window in Water-in-Salt Electrolytes: Understanding the Origins. *J. Am. Chem. Soc.,* 2025, **147**, 35953-35961. (DOI: 10.1021/jacs.5c12989).

7 L. Suo, O. Borodin, T. Gao, M. Olguin, J. Ho, X. Fan, C. Luo, C. Wang and K. Xu, "Water-in-Salt" Electrolyte Enables High-Voltage Aqueous Lithium-Ion Chemistries. *Science,* 2015, **350**, 938–943. (DOI: 10.1126/science.aab1595).

8 Y. Yamada, K. Usui, K. Sodeyama, S. Ko, Y. Tateyama and A. Yamada, Hydrate-Melt Electrolytes for High-Energy-Density Aqueous Batteries. *Nat. Energy,* 2016, **1**, 16129. (DOI: 10.1038/nenergy.2016.129).

9 L. Suo, O. Borodin, W. Sun, X. Fan, C. Yang, F. Wang, T. Gao, Z. Ma, M. Schroeder, A. von Cresce, S. M. Russell, M. Armand, A. Angell, K. Xu and C. Wang, Advanced High-Voltage Aqueous Lithium-Ion Battery Enabled by "Water-in-Bisalt" Electrolyte. *Angew. Chem. Int. Ed.* 2016, **55**, 7136–7141. (DOI: 10.1002/anie.201602397).

10 S. Ko, T. Obukata, T. Shimada, N. Takenaka, M. Nakayama, A. Yamada and Y. Yamada, Electrode potential influences the reversibility of lithium-metal anodes. *Nat. Energy*, 2022, **7**, 1217–1224 (DOI: 10.1038/s41560-022-01144-0).

11 Y. Yamada, K. Furukawa, K. Sodeyama, K. Kikuchi, M. Yaegashi, Y. Tateyama and A. Yamada, Unusual Stability of Acetonitrile-Based Superconcentrated Electrolytes for Fast-Charging Lithium-Ion Batteries. *J. Am. Chem. Soc.*, 2014, **136**, 5039–5046 (DOI: 10.1021/ja412807w).

12 Y. Yamada, Y. Takazawa, K. Miyazaki and T. Abe, Electrochemical Lithium Intercalation into Graphite in Dimethyl Sulfoxide-Based Electrolytes: Effect of Solvation Structure of Lithium Ion. *J. Phys. Chem. C*, 2010, **114**, 11680–11685 (DOI: 10.1021/jp1037427).

13 J. Ming, Z. Cao, W. Wahyudi, M. Li, P. Kumar, Y. Wu, J.-Y. Hwang, M. N. Hedhili, L. Cavallo, Y.-K. Sun and L.-J. Li, New Insights on Graphite Anode Stability in Rechargeable Batteries: Li Ion Coordination Structures Prevail over Solid Electrolyte Interphases. *ACS Energy Lett.*, 2018, **3**, 335–340 (DOI: 10.1021/acsenergylett.7b01177).

14 S.-K. Jeong, H.-Y. Seo, D.-H. Kim, H.-K. Han, J.-G. Kim, Y. B. Lee, Y. Iriyama, T. Abe and Z. Ogumi, Suppression of dendritic lithium formation by using concentrated electrolyte solutions. *Electrochem. Commun.*, 2008, **10**, 635–638 (DOI: 10.1016/j.elecom.2008.02.006).

15 S.-K. Jeong, M. Inaba, Y. Iriyama, T. Abe and Z. Ogumi, Interfacial reactions between graphite electrodes and propylene carbonate-based solutions: Electrolyte-concentration dependence of electrochemical lithium intercalation reaction. *J. Power Sources*, 2008, **175**, 540–546 (DOI: 10.1016/j.jpowsour.2007.08.065).

16 H. Moon, R. Tatara, T. Mandai, K. Ueno, K. Yoshida, N. Tachikawa, T. Yasuda, K. Dokko and M. Watanabe, Mechanism of Li Ion Desolvation at the Interface of Graphite Electrode and Glyme–Li Salt Solvate Ionic Liquids. *J. Phys. Chem. C*, 2014, **118**, 20246–20256 (DOI: 10.1021/jp506772f).

17 N. Takenaka, S. Ko, A. Kitada and A. Yamada, Liquid Madelung Energy Accounts for the Huge Potential Shift in Electrochemical Systems. *Nat. Commun.*, 2024, **15**, 1319 (DOI: 10.1038/s41467-023-44582-4).

18 J. Hu, H. Guo, Y. Li, H. Wang, Z. Wang, W. Huang, L. Yang, H. Chen, Y. Lin and F. Pan, Understanding Li-Ion Thermodynamic and Kinetic Behaviors in Concentrated Electrolyte for the Development of Aqueous Lithium-Ion Batteries. *Nano Energy*, 2021, **89**, 106413 (DOI: 10.1016/j.nanoen.2021.106413).

19 A. Ramanujapuram, D. Gordon, A. Magasinski, B. Ward, N. Nitta, C. Huang and G. Yushin, Degradation and stabilization of lithium cobalt oxide in aqueous electrolytes. *Energy Environ. Sci.*, 2016, **9**, 1841–1848 (DOI: 10.1039/C6EE00093B).

20 J. Kang and H. Lee, Deciphering Potential Shifts in Highly Concentrated LiTFSI Aqueous Electrolytes. *ACS Electrochem.*, 2025, **1**, 419–424 (DOI: 10.1021/acselectrochem.5c00008).

21 H. Koyamada, N. Takenaka, S. Ko, A. Kitada and A. Yamada, Thermodynamics alternative to Debye–Hückel theory. *ChemRxiv*, DOI: 10.26434/chemrxiv-2025-cq36s (2025).

22 W. Wang, V. Balland, M. Branca and B. Limoges, Better Understanding the Role of a Water-in-Salt Electrolyte for Designing a Stable, High-Performance Zinc-Organic Battery. *Chem. Mater.*, 2025, **37**, 8364–8382 (DOI: 10.1021/acs.chemmater.5c02063).

23 F. Yang, J. A. Yuwono, J. Hao, J. Long, L. Yuan, Y. Wang, S. Liu, Y. Fan, S. Zhao, K. Davey and Z. Guo, Understanding H2 Evolution Electrochemistry to Minimize Solvated Water Impact on Zinc-Anode Performance. *Adv. Mater.*, 2022, **34**, 2206754 (DOI: 10.1002/adma.202206754).

24 F. W. Fenta and R. Bouchal, Unraveling the significance of the zinc ratio in water-in-salt electrolytes. *J. Mater. Chem. A*, 2024, **12**, 25035–25046 (DOI: 10.1039/D4TA02704C).

25 A. Rana, K. Roy, J. N. Heil, J. H. Nguyen, C. Renault, B. M. Tackett and J. E. Dick, Realizing the Kinetic Origin of Hydrogen Evolution for Aqueous Zinc Metal Batteries. *Adv. Energy Mater.*, 2024, **14**, 2402521 (DOI: 10.1002/aenm.202402521).

26 J. Liu, T. M. Webb, J. Ortiz-Castillo and T. Gao, Thermodynamics of transition metal electrodeposition in concentrated aqueous electrolytes. *ChemRxiv*, DOI: 10.26434/chemrxiv-2025-78gps (2025).

27 H. Iriawan, A. Herzog, S. Yu, N. Ceribelli and Y. Shao-Horn, Upshifting Lithium Plating Potential To Enhance Electrochemical Lithium Mediated Ammonia Synthesis. *ACS Energy Lett.*, 2024, **9**, 4883–4891 (DOI: 10.1021/acsenergylett.4c02149).

28 J. Tang, B. Huang, X. Xiao, H. Qu, Y. Song, J. Li, Y. Song, H. Ji, J. Wang, Y. Zhu and G. Zhou, Water-in-Salt Solution for Direct Regeneration of Degraded Lithium Iron Phosphate. *J. Am. Chem. Soc.*, 2025, **147**, 24594–24603 (DOI: 10.1021/jacs.5c05384).

29 H. Zhang, D. Raciti and A. S. Hall, Disordered interfacial H_2O promotes electrochemical C–C coupling. *Nat. Chem.*, 2025, **17**, 1161–1168 (DOI: 10.1038/s41557-025-01859-z).

30 D. Degoulange, N. Dubouis and A. Grimaud, Toward the understanding of water-in-salt electrolytes: Individual ion activities and liquid junction potentials in highly concentrated aqueous solutions. *J. Chem. Phys.*, 2021, **155**, 064701 (DOI: 10.1063/5.0058506).

31 B. Ernould, L. Sieuw, G. Barozzino-Consiglio, J.-F. Gohy and A. Vlad, Negative Redox Potential Shift in Fire-Retardant Electrolytes and Consequences for High-Energy Hybrid Batteries. *ACS Appl. Energy Mater.*, 2019, **2**, 7879–7885 (DOI: 10.1021/acsaem.9b01339).

32 P. M. May and E. F. May, Junction potentials in electrochemical cells with transference: A review and prescription to end over 70 years of sleepwalking. *Electrochim. Acta*, 2025, **539**, 147087 (DOI: 10.1016/j.electacta.2025.147087).

33 K. Ueno, R. Tatara, S. Tsuzuki, S. Saito, H. Doi, K. Yoshida, T. Mandai, M. Matsugami, Y. Umebayashi, K. Dokko and M. Watanabe, Li^+ solvation in glyme–Li salt solvate ionic liquids. *Phys. Chem. Chem. Phys.*, 2015, **17**, 8248–8257 (DOI: 10.1039/C4CP05943C).

34 P. K. R. Kottam, D. Kalkan, M. Wohlfahrt-Mehrens and M. Marinaro, Influence of Li-Salt Concentration on Redox Potential of Lithium Metal and Electrochemistry of Ferrocene in DMSO-Based Electrolytes. *J. Electrochem. Soc.*, 2019, **166**, A1574–A1579 (DOI: 10.1149/2.0881908jes).

35 R. Tatara, K. Ueno, K. Dokko and M. Watanabe, Thermodynamic Effect of Anion Activity on Electrochemical Reactions Involving Li^+ Ions in Room-Temperature Ionic Liquids. *ChemElectroChem*, 2019, **6**, 4444–4449 (DOI: 10.1002/celc.201900973).

36 R. Andreu, M. Sluyters-Rehbach, A. G. Remijnse and J. H. Sluyters, The mechanism of the reduction of Zn(II) from $NaClO_4$ base electrolyte solutions at the DME. *J. Electroanal. Chem.*, 1982, **134**, 101–115 (DOI: 10.1016/0022-0728(82)85030-4).

37 H. W. Harper, Calculation of liquid junction potentials. *J. Phys. Chem.*, 1985, **89**, 1659–1664 (DOI: 10.1021/j100255a022).

38 J. Bagg, Computer calculation of liquid-junction potentials—II. Junction potentials for junctions with concentrated KCl. *Electrochim. Acta*, 1990, **35**, 367–370 (DOI: 10.1016/0013-4686(90)87012-Q).

39 Y. Wang, W. Zhu, K. Lin, L. Yuan, X. Zhou and S. Liu, Ratiometric Detection of Raman Hydration Shell Spectra. *J. Raman Spectrosc.*, 2016, **47**, 1231–1238 (DOI: 10.1002/jrs.4940).

40 A. D. Wilson and C. Stetson, Modeling solution vapor equilibria with solvation and solute assembly. *J. Mol. Liq.*, 2021, **336**, 116272 (DOI: 10.1016/j.molliq.2021.116272).

41 A. D. Wilson, M. Arrad and A. S. Wexler, Step-wise Hydration: Comparison of Debye-Hückel Long-Range interactions and ion pairing. *J. Mol. Liq.*, 2025, **431**, 127805 (DOI: 10.1016/j.molliq.2025.127805).

42 A. D. Wilson, H. Lee and C. Stetson, Mass action model of solution activity via speciation by solvation and ion pairing equilibria. *Commun. Chem.*, 2021, **4**, 163 (DOI: 10.1038/s42004-021-00599-8).

43 N. Makivic, J.-Y. Cho, K. D. Harris, J.-M. Tarascon, B. Limoges and V. Balland, Evidence of Bulk Proton Insertion in Nanostructured Anatase and Amorphous TiO_2 Electrodes. *Chem. Mater.*, 2021, **33**, 3436–3448 (DOI: 10.1021/acs.chemmater.1c00840).

44 N. Makivic, K. D. Harris, J.-M. Tarascon, B. Limoges and V. Balland, Impact of reversible proton insertion on the electrochemistry of electrode materials operating in mild aqueous electrolytes: a case study with TiO_2. *Adv. Energy Mater.*, 2023, **13**, 2203122 (DOI: 10.1002/aenm.202203122).

45 W. J. Hamer and Y.-C. Wu, Osmotic Coefficients and Mean Activity Coefficients of Uni-univalent Electrolytes in Water at 25°C. *J. Phys. Chem. Ref. Data*, 1972, **1**, 1047–1100 (DOI: 10.1063/1.3253108).

46 H. Ohtaki and T. Radnai, Structure and Dynamics of Hydrated Ions. *Chem. Rev.*, 1993, **93**, 1157–1204 (DOI: 10.1021/cr00019a014).

47 H. H. L. and B. M. R., The hydration structure of the lithium ion. *J. Chem. Phys.*, 2002, **117**, 110–117 (DOI: 10.1063/1.1480875).

48 R. Wolfram, H. B. Murray and C. P. Cory, Hydration of Lithium Ion in Aqueous Solution. *J. Phys. Chem.*, 1995, **99**, 3793–3797 (DOI: 10.1021/j100011a055).

49 J. L. Green, A. R. Lacey and M. G. Sceats, Determination of the total hydration number of a LiCl cation-anion pair via collective proton motions. *Chem. Phys. Lett.*, 1987, **134**, 385–391 (DOI: 10.1016/0009-2614(87)87158-0).

50 Y. Marcus, *Ion Solvation*, Wiley, New York, 1985.

51 J. F. Hinton and E. S. Amis, Solvation numbers of ions. *Chem. Rev.*, 1971, **71**, 627–674 (DOI: 10.1021/cr60274a003).

52 Y. Marcus, Concentration Dependence of Ionic Hydration Numbers. *J. Phys. Chem. B*, 2014, **118**, 10471–10476 (DOI: 10.1021/jp5039255).

53 B. M. Rode, C. F. Schwenk and A. Tongraar, Structure and dynamics of hydrated ions — new insights through quantum mechanical simulations. *J. Mol. Liq.*, 2004, **110**, 105–122 (DOI: 10.1016/j.molliq.2003.09.016).

54 A. Tot and L. Kloo, Water-in-salt electrolytes – molecular insights to the high solubility of lithium-ion salts. *Chem. Commun.*, 2022, **58**, 9528–9531 (DOI: 10.1039/D2CC03062D).

55 Q. Sun, The Raman OH stretching bands of liquid water. *Vib. Spectrosc.*, 2009, **51**, 213–217. (DOI: 10.1016/j.vibspec.2009.05.002)

56 J. Gujt, M. Bešter-Rogač and B. Hribar-Lee, An investigation of ion-pairing of alkali metal halides in aqueous solutions using the electrical conductivity and the Monte Carlo computer simulation methods. *J. Mol. Liq.*, 2014, **190**, 34–41. (DOI: 10.1016/j.molliq.2013.09.025)

57 L. Suo, F. Han, X. Fan, H. Liu, K. Xu and C. Wang, "Water-in-Salt" electrolytes enable green and safe Li-ion batteries for

View Article Online
DOI: 10.1039/D6SC00393A

large scale electric energy storage applications. *J. Mater. Chem. A*, 2016, **4**, 6639–6644 (DOI: 10.1039/C6TA00451B).

58 M. Turgeman, V. Wineman-Fisher, F. Malchik, A. Saha, G. Bergman, B. Gavriel, T. R. Penki, A. Nimkar, V. Baranauskaite, H. Aviv, M. D. Levi, M. Noked, D. T. Major, N. Shpigel and D. Aurbach, A cost-effective water-in-salt electrolyte enables highly stable operation of a 2.15-V aqueous lithium-ion battery. *Cell Rep. Phys. Sci.*, 2022, 100688 (DOI: 10.1016/j.xcrp.2021.100688).

View Article Online
DOI: 10.1039/D6SC00393A

Data availability

The data supporting this article have been included as part of the Supplementary Information. Supplementary information (SI): Raman analysis, Tables S1 and S2, Figures S1 and S2. The data and calculations that support the findings of this study are available from the corresponding author upon request.